

UC Berkeley

UC Berkeley Previously Published Works

Title

Programmable Heisenberg interactions between Floquet qubits

Permalink

<https://escholarship.org/uc/item/4g724604>

Journal

Nature Physics, 20(2)

ISSN

1745-2473

Authors

Nguyen, Long B

Kim, Yosep

Hashim, Akel

et al.

Publication Date

2024-02-01

DOI

10.1038/s41567-023-02326-7

Copyright Information

This work is made available under the terms of a Creative Commons Attribution License, available at <https://creativecommons.org/licenses/by/4.0/>

Peer reviewed



Programmable Heisenberg interactions between Floquet qubits

Received: 27 November 2022

Accepted: 7 November 2023

Published online: 16 January 2024

 Check for updates

Long B. Nguyen ^{1,2,8} ✉, Yosep Kim ^{1,2,3,7,8} ✉, Akel Hashim ^{1,2}, Noah Goss ^{1,2}, Brian Marinelli ^{1,2}, Bibek Bhandari ⁴, Debmalya Das ^{4,5}, Ravi K. Naik ^{1,2}, John Mark Kreikebaum ^{2,6}, Andrew N. Jordan ^{4,5}, David I. Santiago ^{1,2} & Irfan Siddiqi^{1,2,6}

The trade-off between robustness and tunability is a central challenge in the pursuit of quantum simulation and fault-tolerant quantum computation. In particular, quantum architectures are often designed to achieve high coherence at the expense of tunability. Many current qubit designs have fixed energy levels and consequently limited types of controllable interactions. Here by adiabatically transforming fixed-frequency superconducting circuits into modifiable Floquet qubits, we demonstrate an XXZ Heisenberg interaction with fully adjustable anisotropy. This interaction model can act as the primitive for an expressive set of quantum operations, but is also the basis for quantum simulations of spin systems. To illustrate the robustness and versatility of our Floquet protocol, we tailor the Heisenberg Hamiltonian and implement two-qubit iSWAP, CZ and SWAP gates with good estimated fidelities. In addition, we implement a Heisenberg interaction between higher energy levels and employ it to construct a three-qubit CCZ gate, also with a competitive fidelity. Our protocol applies to multiple fixed-frequency high-coherence platforms, providing a collection of interactions for high-performance quantum information processing. It also establishes the potential of the Floquet framework as a tool for exploring quantum electrodynamics and optimal control.

The capability to coherently choreograph interactions between qubits is the foundation for the recent advances in quantum technologies. A quintessential example is the manipulation of the quantum Heisenberg model for the simulation of many-body quantum spin systems^{1–4}, which has led to the recent discoveries of intriguing physical phenomena such as discrete time crystal⁵, phantom spin-helix states⁶ and formation of photon bound states⁷. The Heisenberg interactions are also the primitives for expressive multi-qubit gates⁸ which play important roles in quantum algorithms⁹ and quantum error correction^{10,11}. Therefore, endowing quantum architectures with such archetypal interactions considerably extends their capabilities and performance.

The required tunability in solid-state quantum devices entails additional decoherence channels, demanding design overhead and increased operational complexity. For example, in the domain of superconducting circuits, the performance in flux-tunable devices is typically limited by unavoidable $1/f$ noise arising from the surrounding environment. Meanwhile, fixed-frequency platforms such as single-junction transmon^{12,13} and fluxonium¹⁴ biased at the half-integer flux quantum¹⁵ have the best coherence times to date, but their native interactions are limited to the cross-resonance^{16,17} and longitudinal couplings^{18,19}. Parametric longitudinal^{20–22} and transverse interactions²³ can also be accomplished by introducing additional tunable couplers,

¹Computational Research Division, Lawrence Berkeley National Laboratory, Berkeley, CA, USA. ²Department of Physics, University of California, Berkeley, CA, USA. ³Center for Quantum Information, Korea Institute of Science and Technology (KIST), Seoul, Korea. ⁴Institute for Quantum Studies, Chapman University, Orange, CA, USA. ⁵Department of Physics and Astronomy, University of Rochester, Rochester, NY, USA. ⁶Materials Science Division, Lawrence Berkeley National Laboratory, Berkeley, CA, USA. ⁷Present address: Department of Physics, Korea University, Seoul, Korea. ⁸These authors contributed equally: Long B. Nguyen, Yosep Kim. ✉e-mail: longbnguyen@berkeley.edu; yosep9201@gmail.com

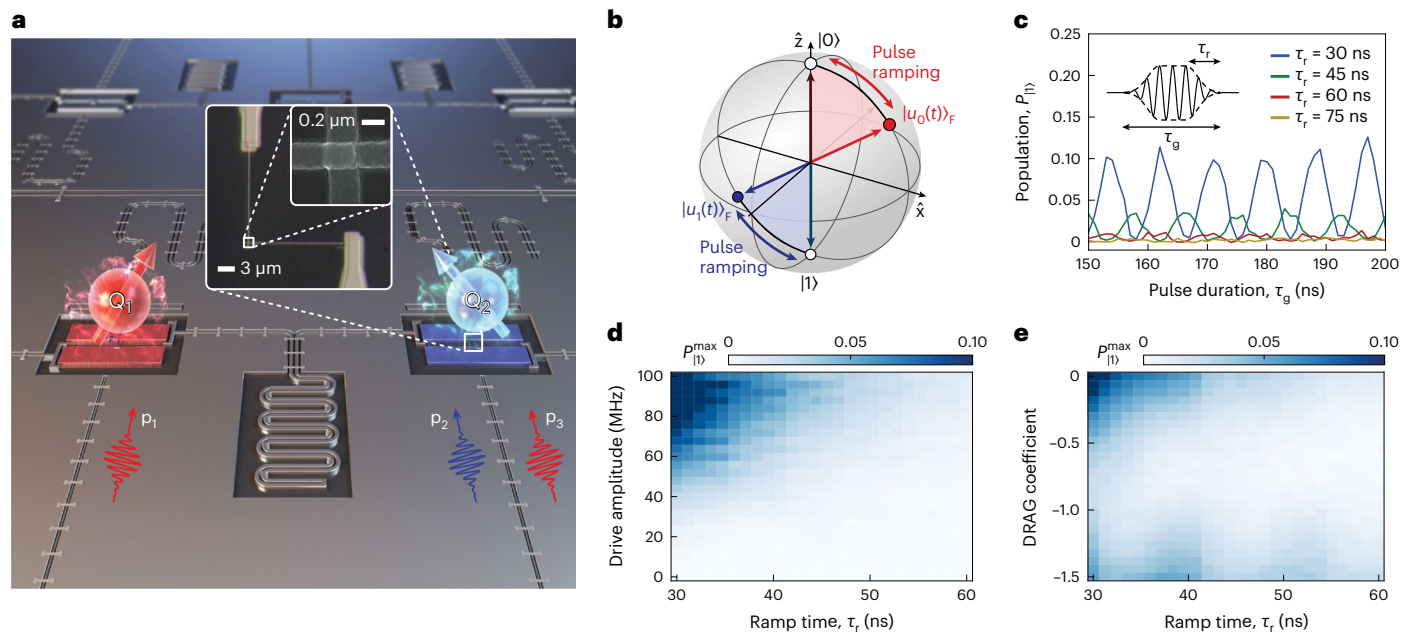


Fig. 1 | Floquet qubit. **a**, Experimental schematic depicting two single-junction transmon qubits Q_1 (red) and Q_2 (blue) coupled via a shared coplanar stripline resonator resulting in an effective static coupling³¹. Microwave pulses are applied to the transmission lines situated below the capacitor pads to sculpt the Floquet qubits and control single-qubit rotations. The Heisenberg interactions are programmed by tailoring pulses p_1 , p_2 and p_3 . **b**, Bloch-sphere representation of the adiabatic transformation from a bare qubit in the lab frame to a Floquet qubit

in the rotating frame. **c**, Population in the excited state P_{11} of Q_1 , initially in $|0\rangle$, when subjected to a microwave pulse with amplitude 100 MHz, detuning -40 MHz, ramp time τ_r and duration τ_g . Non-adiabaticity manifests as finite oscillations for short ramp time τ_r . **d**, Dependence of the maximum state leakage P_{11}^{\max} on the pulse's amplitude and ramp time τ_r . The drive is applied at the same frequency as in **c**. **e**, Dependence of P_{11}^{\max} on the pulse's ramp time τ_r and DRAC coefficient. The drive amplitude and frequency are the same as in **c**.

but the performance could be undermined by the couplers' coherence and spurious couplings.

In this Article, we present a reliable and hardware-efficient protocol to synthesize Floquet qubits^{24–26} from statically coupled single-junction transmon qubits using time-periodic microwave drives, showing that the adiabatic mapping procedure can be hastened by exploiting a shortcuts-to-adiabaticity (STA) technique^{27–29}. Then, we implement an XXZ Heisenberg interaction between these Floquet qubits, described by the Hamiltonian

$$\frac{\mathcal{H}_{\text{XXZ}}}{\hbar} = \sum_{i,j} J_{XY} (\hat{\sigma}_x^i \hat{\sigma}_x^j + \hat{\sigma}_y^i \hat{\sigma}_y^j) + J_{ZZ} \hat{\sigma}_z^i \hat{\sigma}_z^j \quad (1)$$

and demonstrate that the transverse spin-exchange and longitudinal spin–spin interaction terms can be adjusted independently by tailoring the drive parameters.

To validate the robustness and practicality of the protocol, we characterize two-qubit iSWAP, CZ and SWAP gates which correspond to different anisotropy $\Delta = J_{ZZ}/J_{XY}$ values, achieving estimated fidelities of 99.32(3)%, 99.72(2)% and 98.93(5)%, respectively. In addition, we show that the Floquet-engineered interactions can be broadly applied to other levels in the system. Specifically, we explore the swapping between the qutrit states $|11\rangle$ and $|02\rangle$, then employ it to implement a three-qubit controlled-controlled-Z (CCZ) gate which is locally equivalent to the Toffoli gate³⁰, achieving an estimated fidelity of 96.18(5)%. Our work exemplifies the operational principles of Floquet qubits and illustrates their broad potential, thus opening promising pathways for future developments of the Floquet framework in enhancing the capabilities of fixed-frequency solid-state quantum platforms.

Synthesizing Floquet qubits

Figure 1a depicts the superconducting device used as a testbed in the experiment. It consists of single-junction transmon qubits¹² that are pair-wise coupled via mutual coplanar stripline resonators^{31,32}.

Details of the quantum device and experimental setup are presented in Supplementary Notes 1 and 2. Although the frequencies of the qubits are fixed after fabrication, Floquet engineering has recently emerged as a powerful tool that allows the sculpting of effective Hamiltonians that are otherwise unavailable³³, thus promising an additional dimension to tune the system. Here, we synthesize Floquet qubits using detuned periodic microwave drives and tailor them to implement the Hamiltonian given by equation (1).

The mapping is described by Floquet formalism as follows. The Hamiltonian of a two-level spin-half system subjected to a periodic driving field with amplitude A , frequency ω_d and phase φ is given as

$$\frac{\mathcal{H}_q(t)}{\hbar} = -\frac{\omega_q}{2} \hat{\sigma}_z + A \cos(\omega_d t + \varphi) \hat{\sigma}_x, \quad (2)$$

where $\hbar\omega_q$ is the energy gap of the two-level system, and $\hat{\sigma}_z$ and $\hat{\sigma}_x$ represent the Pauli operators. There exists no static eigenenergies and eigenstates of the system as solutions of the time-dependent Schrödinger equation $i\hbar\partial_t |\psi(t)\rangle = \mathcal{H}_q(t) |\psi(t)\rangle$. However, due to the periodicity of $\mathcal{H}_q(t)$, the Schrödinger equation can be modified into the Floquet equation^{34,35} $(\mathcal{H}_q(t) - i\hbar\partial_t) |u_n(t)\rangle_F = \hbar\varepsilon_n |u_n(t)\rangle_F$, and static quasienergies $\hbar\varepsilon_n$ can be found for time-periodic Floquet states $|u_n(t)\rangle_F = |u_n(t + 2\pi/\omega_d)\rangle_F$. Here, the Floquet states are denoted with subscript F to distinguish them from the bare states in the lab frame. The Floquet and bare states are interconvertible following the relation

$$|u_n(t)\rangle_F = e^{i\varepsilon_n t} |\psi_n(t)\rangle. \quad (3)$$

Interestingly, $e^{ik\omega_d t} |u_n(t)\rangle_F$ with integer k also satisfies the Floquet equation and has quasienergy $\hbar(\varepsilon_n + k\omega_d)$, resulting in an infinite transition spectrum³⁵ $\varepsilon_1 - \varepsilon_0 = k\omega_d \pm \sqrt{A^2 + (\omega_d - \omega_q)^2}$, where the plus(minus) sign corresponds to red(blue)-detuned drive. In addition, the drive phase φ acts as a time translation operator on the Hamiltonian in equation (2), $|u_n(t)\rangle_F \rightarrow |u_n(t + \varphi/\omega_d)\rangle_F$. These show how the Floquet states

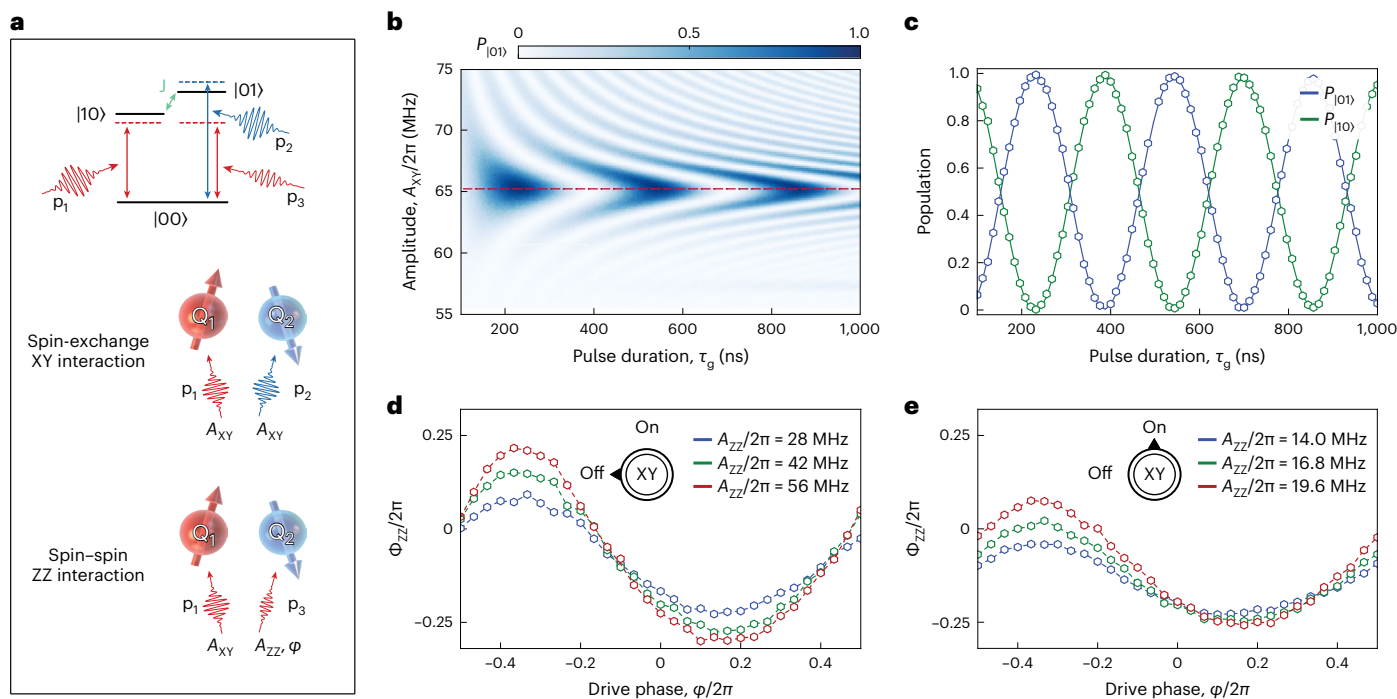


Fig. 2 | Floquet-engineered XXZ Heisenberg interaction. **a**, Energy diagram of qubits Q_1 and Q_2 and pulse schematics for spin-exchange XY and spin-spin ZZ interactions. **b**, Chevron pattern showing the dependence of $P_{|01\rangle}$ on the amplitude A_{XY} and duration τ_g of pulses p_1 and p_2 for qubits initialized in $|10\rangle$. The pulses are applied at frequencies 40 MHz red(blue)-detuned from $Q_{1(2)}$'s $|0\rangle \leftrightarrow |1\rangle$ transition with DRAG coefficients $\lambda_{\text{DRAG}} = -(+)0.6$ and ramp time $\tau_r = 50$ ns. **c**, Coherent oscillation between $|10\rangle$ and $|01\rangle$ for the optimal pulse amplitude $A_{XY}/2\pi = 65.2$ MHz highlighted by the red dashed line in **b**. **d**, Extracted

longitudinal coupling angle Φ_{ZZ} between the qubits after p_1 and p_3 are applied at 40 MHz red-detuned from Q_1 's transition frequency. They are 200 ns long, with ramp time $\tau_r = 50$ ns and DRAG coefficient $\lambda_{\text{DRAG}} = -0.6$. The amplitude of p_1 is fixed at $A_{XY}/2\pi = 65.2$ MHz, while the amplitude A_{ZZ} and phase φ of p_3 are varied to tune the ZZ coupling rate. **e**, Extracted longitudinal coupling angle Φ_{ZZ} between the qubits after being subjected to all three pulses. The amplitude A_{XY} of p_1 and p_2 is tuned to induce a full $|10\rangle \leftrightarrow |01\rangle$ swap, while the amplitude A_{ZZ} and phase φ of p_3 are varied to tune the ZZ rate during the swap.

and their quasienergies depend on the drive parameters A , φ and ω_d , which we can use to tailor the driven systems (see Supplementary Notes 3 and 4 for detailed Floquet formalism).

To prepare a Floquet qubit with the desired properties, we have to continuously map the undriven qubit to the Floquet basis, as shown in Fig. 1b. If the transformation is performed abruptly, finite tunnelling exists between the Floquet basis states, and the process becomes non-adiabatic. According to the Adiabatic Theorem³⁵, the tunnelling rate is proportional to dA/dt , that is, the target Floquet qubit corresponding to a larger drive amplitude must be transformed using a longer ramp time.

We experimentally explore this by irradiating qubit Q_1 initialized in $|0\rangle$ using a cosine-ramp pulse with different pulse durations τ_g and ramp times τ_r . The drive amplitude is set to be 100 MHz in terms of on-resonant Rabi frequency, and the drive frequency is red-detuned by 40 MHz from Q_1 's transition frequency. As the qubit should remain in its instantaneous eigenstate under the adiabatic process, non-adiabatic effects manifest as finite excited state populations $P_{|1\rangle}$ after the pulse, which oscillates with respect to the pulse duration due to the dynamical phase accumulation of the Floquet qubit (Fig. 1c). Evidently, shorter ramp times correspond to more severe non-adiabatic effects. In addition, the result in Fig. 1d confirms that a larger drive amplitude requires a longer ramp time to satisfy the adiabatic condition.

Interestingly, we find that using an STA technique known as derivative removal by adiabatic gate (DRAG)^{28,29} helps reduce non-adiabatic effects substantially. As shown in Fig. 1e, the excited state leakage $P_{|1\rangle}^{\text{max}}$ corresponding to a short-ramp pulse can be suppressed by adding a quadrature component to the pulse with amplitude $A_0 = \lambda_{\text{DRAG}} \times dA(t)/dt$. In this case, τ_r can be reduced from 60 ns to 30 ns by employing a DRAG coefficient $\lambda_{\text{DRAG}} = -0.7$. This suggests that advanced optimal

control techniques can be explored to further accelerate the mapping procedure. Importantly, our results below show that once adiabaticity is satisfied, the protocol is robust against adverse effects from the strong drives, including microwave crosstalk, calibration fluctuations and leakage to higher levels.

Tailoring Heisenberg interactions

Having established the general conditions for adiabatic mapping between undriven qubit states and Floquet states, we next generate the microwave pulses that establish the XXZ Heisenberg interaction in equation (1) between the Floquet qubits. The interaction Hamiltonian describing the coupling between Q_1 and Q_2 in Fig. 1a is $\mathcal{H}_{\text{int}}/\hbar = J\sigma_x^{(1)}\sigma_x^{(2)}$, where J is the static coupling strength, the superscripts are qubit indices, and the Pauli operators are defined in the undriven basis. Using the relation given by equation (3), this interaction can be described by a Floquet Hamiltonian:

$$\frac{\mathcal{H}_{\text{int},F}}{\hbar} = J \sum_{a,b,c,d} c_{ab}^{(1)}(t)c_{cd}^{(2)}(t)e^{i(\varepsilon_{ab}^{(1)} + \varepsilon_{cd}^{(2)})t} f_{ab}^{(1)}(t)f_{cd}^{(2)}(t), \quad (4)$$

where $\varepsilon_{ab}^{(k)} \equiv \varepsilon_b^{(k)} - \varepsilon_a^{(k)}$, $c_{ab}^{(k)}(t) = \langle \psi_a^{(k)}(t) | \sigma_x^{(k)} | \psi_b^{(k)}(t) \rangle$, $f_{ab}^{(k)}(t) = |u_a^{(k)}(t)\rangle_F \langle u_b^{(k)}(t)|_F$ for qubit Q_k and $a, b, c, d \in \{0, 1\}$ for two qubits. The fast oscillation dynamics can be neglected by invoking the rotating wave approximation, leaving only the terms that follow energy conservation law, $\varepsilon_{ab}^{(1)} + \varepsilon_{cd}^{(2)} = 0$ for $abcd \in \{0110, 1001, 0000, 0011, 1100, 1111\}$. Inspecting the reduced Hamiltonian then gives us insight on the types of interactions present between the qubits.

On one hand, the terms satisfying $\varepsilon_{01}^{(1)} = \varepsilon_{01}^{(2)}$ correspond to the transverse XY spin-exchange interaction in equation (1) with

$J_{XY} = J\langle c_{01}^{(1)} c_{10}^{(2)} \rangle_t = J\langle c_{10}^{(1)} c_{01}^{(2)} \rangle_t$, where $\langle \dots \rangle_t$ denotes the time-average value. This process follows the conventional wisdom that an XY exchange-type interaction between two coupled spins occurs when they are brought into resonance with each other. On the other hand, the rest of the reduced Hamiltonian produces the longitudinal ZZ spin–spin coupling in equation (1), $J_{ZZ} = J\langle c_{11}^{(1)} c_{11}^{(2)} + c_{00}^{(1)} c_{00}^{(2)} - c_{00}^{(1)} c_{11}^{(2)} - c_{11}^{(1)} c_{00}^{(2)} \rangle_t$. Consequently, we can program the transverse and longitudinal interactions independently by tailoring the quasienergies with periodic microwave drives.

We validate this principle as follows. First, we achieve a pure transverse XY spin-exchange interaction corresponding to an XX Heisenberg model where the anisotropy is zero, $\Delta = J_{ZZ}/J_{XY} = 0$. Given that Q_1 's frequency is lower than that of Q_2 , their quasienergy differences $\epsilon_{01}^{(k)}$ can be brought into resonance if $Q_1(Q_2)$ is driven with red(blue)-detuned microwaves (Supplementary Note 5). After preparing the qubits in $|10\rangle$, we apply two such pulses (p_1 and p_2 in Fig. 2a) with the same duration τ_g and amplitude A_{XY} at a detuning frequency of 40 MHz.

We observe a coherent population transfer to state $|01\rangle$ that forms a chevron pattern as a function of τ_g and A_{XY} , signifying a transverse coupling between the qubits (Fig. 2b). Notably, although the interaction occurs between the Floquet qubits in the dressed frame, the adiabatic connection ascertains the exchange between the bare qubit states after the reverse mapping, which bears resemblance to the latching mechanism in classical electronics. Indeed, at the optimal drive amplitude $A_{XY}/2\pi = 65.2$ MHz (Fig. 2c), $|10\rangle$ and $|01\rangle$ exhibit coherent oscillations at a rate of 3.2 MHz, which is limited by the static coupling constant J (Supplementary Note 5). The lack of fast oscillatory behaviour is a clear indication of the high mapping fidelity.

Next, we induce a pure longitudinal ZZ spin–spin coupling corresponding to an Ising interaction between the Floquet qubits. This can be accomplished by irradiating microwave drives p_1 on Q_1 and p_3 on Q_2 (Fig. 2a) at a frequency 40 MHz red-detuned from Q_1 . The amplitude of p_1 is fixed at $A_{XY}/2\pi = 65.2$ MHz, while p_3 has parameterized amplitude A_{ZZ} and phase φ . For weak driving, $A_{XY,ZZ} \ll \omega_{q,d}$, the ZZ rate is given as

$J_{ZZ} \approx 2J_{XY}A_{ZZ} \cos(\varphi) / \sqrt{(A_{XY}^2 + \delta_1^2)(A_{ZZ}^2 + \delta_2^2)}$, where δ_k is the detuning from Q_k 's frequency (Supplementary Note 5). Importantly, while the transverse coupling rate J_{XY} shown above is limited by the static coupling strength J , the longitudinal coupling rate J_{ZZ} can be tuned by two knobs, namely the drives' amplitudes and phase difference. We characterize the interaction by first initializing the two qubits in the superposition state $(|0\rangle + |1\rangle) \otimes (|0\rangle + |1\rangle)/2$, applying the pulses as specified and then extracting the entangling phase $\Phi_{ZZ}(\tau_g) = \int_0^{\tau_g} J_{ZZ}(t) dt$ using tomographic reconstruction assisted by numerical optimization. As shown in Fig. 2d, this phase depends on p_3 's amplitude A_{ZZ} and phase φ , consistent with our description.

Leveraging the independent controls of the transverse and longitudinal interactions, we now tailor the interplay between them to adjust the anisotropy of the XXZ Heisenberg interaction model. To this end, we apply p_1 and p_2 pulses with their amplitude A_{XY} and duration τ_g tuned to induce a full $|10\rangle \leftrightarrow |01\rangle$ swap (Fig. 2c). Pulse p_3 is then jointly applied, albeit with parameterized amplitude A_{ZZ} and phase φ . Incorporating the swap condition into the tomography analysis, we extract the longitudinal entangling phase Φ_{ZZ} which depends on p_3 's parameters as shown in Fig. 2e. This demonstrates the versatility available in programming the anisotropy of the model given by equation (1). This demonstration only includes $A_{ZZ} \lesssim 20$ MHz to alleviate the effect from p_3 on the swap condition, which stems from the large microwave crosstalk in the experimental device (Supplementary Note 2).

Benchmarking Heisenberg interactions

The programmable Heisenberg interaction endows quantum processors with an extensive quantum gate set and the capability to simulate many-body spin-half systems. Here we benchmark our Floquet-engineered Heisenberg interactions by characterizing a suite

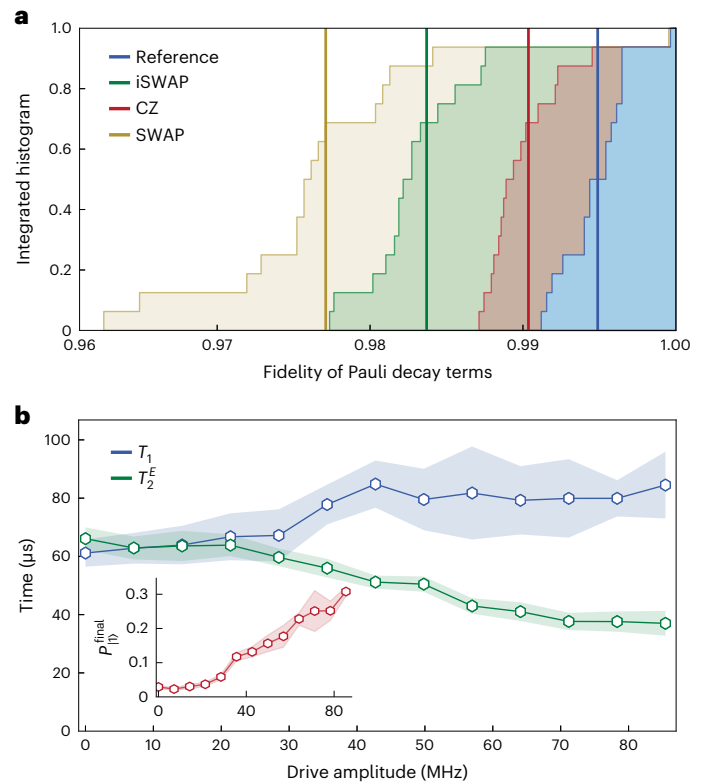


Fig. 3 | Characterization of two-qubit gates. a, CB results showing the Pauli fidelity histogram for the Reference, iSWAP, CZ and SWAP cycles, with the solid vertical lines indicating the mean values. The corresponding two-qubit gate fidelities are estimated to be 99.32(3)%, 99.72(2)% and 98.93(5)%, respectively. **b**, Effective coherence time statistics of the Floquet qubit created by adiabatically driving Q_1 at a red-detuning of 40 MHz. Each curve shows the mean values of 20 different sweeps, and the shaded region represents the standard deviations. Inset: Excited state population at the end of the 355- μs -long $|10\rangle \rightarrow |1\rangle$ measurement sequence.

of representative two-qubit gates: the iSWAP, CZ and SWAP gates resulting from the XX Heisenberg model $\mathcal{H}_{XX}/\hbar = J_{XY}(\hat{\sigma}_x \hat{\sigma}_x + \hat{\sigma}_y \hat{\sigma}_y)$, Ising model $\mathcal{H}_{ZZ}/\hbar = J_{ZZ} \hat{\sigma}_z \hat{\sigma}_z$ and XXX Heisenberg model $\mathcal{H}_{XXX}/\hbar = J(\hat{\sigma}_x \hat{\sigma}_x + \hat{\sigma}_y \hat{\sigma}_y + \hat{\sigma}_z \hat{\sigma}_z)$, respectively. Accordingly, an iSWAP unitary arises naturally from a pure transverse XY interaction with the pulse duration τ_g corresponding to a full swap in Fig. 2c, implemented by applying p_1 and p_2 . In practice, there is a dynamical ZZ coupling originating from microwave crosstalk, which can be tracked and compensated by simultaneously applying p_3 with appropriate amplitude and phase. Likewise, a CZ gate is realized when p_1 and p_3 are calibrated to bring up an entangling phase $\Phi_{ZZ}/2\pi = 0.25$. Finally, we tailor all three pulses to sculpt an isotropic XXX Heisenberg interaction that leads to a SWAP gate at the correct gate time τ_g , at which both iSWAP and CZ conditions are satisfied. Our calibration steps are detailed in Supplementary Notes 6–8.

To quantify the gates' performances without state preparation and measurement errors, we employ cycle benchmarking (CB)³⁶, which tailors all errors into stochastic Pauli channels via Pauli twirling and results in tight bounds on the estimated fidelity (Supplementary Note 9). Besides the dressed cycles that include the implemented gates, we also measure the reference cycle and extract its errors to estimate the relevant gate fidelities. Figure 3a shows the Pauli fidelity distribution histograms of both the reference and dressed cycles corresponding to the intended two-qubit gates. Comparing the dressed cycle data to the reference cycle result allows us to estimate the average gate fidelities of the implemented iSWAP, CZ and SWAP gates to be 99.32(3)%, 99.72(2)% and 98.93(5)%, respectively. We note that these gates are expandable

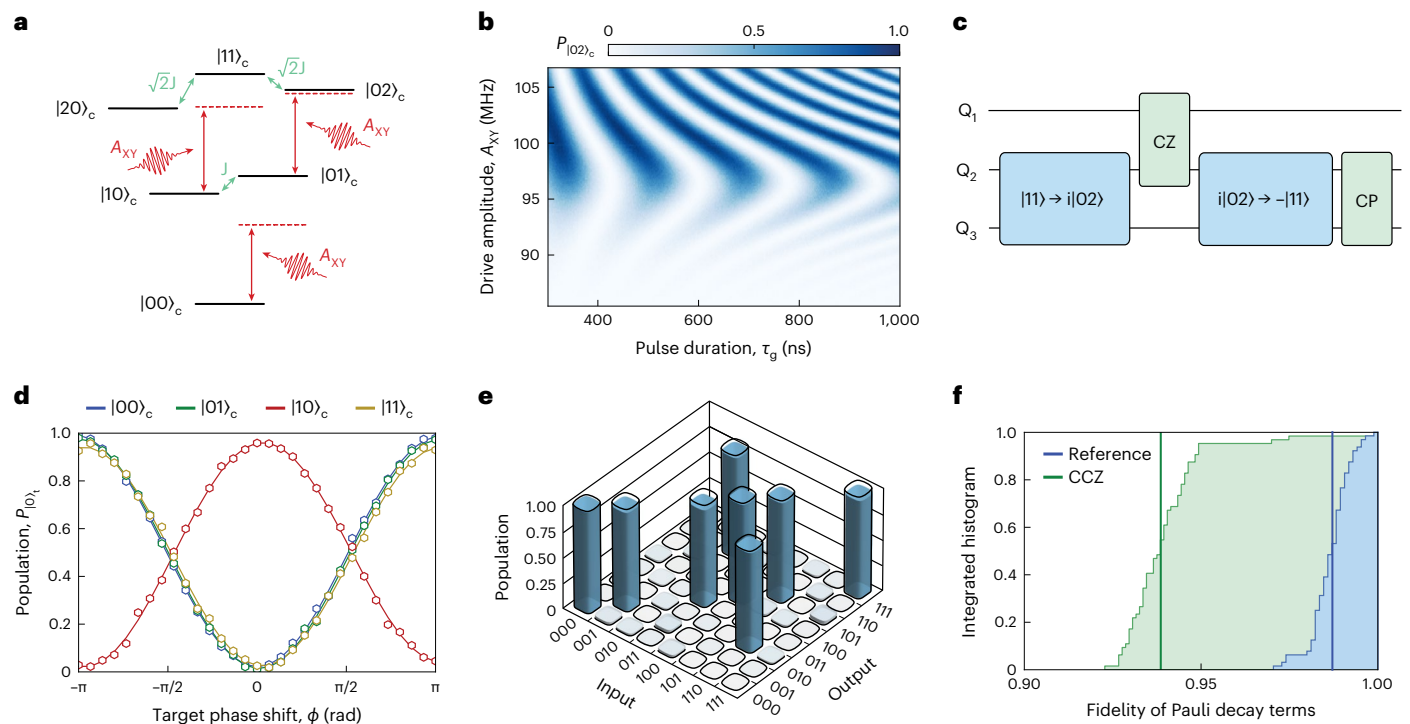


Fig. 4 | Floquet qutrit and three-qubit CCZ gate. a, Energy diagram of two coupled transmon circuits Q_2 and Q_3 , with the subscript c denoting they are control qubits. A microwave drive with amplitude A_{XY} is applied at a frequency red-detuned from Q_3 's $|1\rangle \leftrightarrow |2\rangle$ transition to create a Floquet qutrit. **b**, Chevron pattern showing a coherent flip-flop between Q_2 and Q_3 's states $|11\rangle_c$ and $|02\rangle_c$, which depends on the amplitude A_{XY} and duration τ_g of the pulse. The red-detuning is 22 MHz, the ramp time is $\tau_r = 170$ ns and the DRAG coefficient is $\lambda_{\text{DRAG}} = -0.6$. **c**, Gate sequence used to implement a three-qubit CCZ unitary, with Q_1 as the target qubit and Q_2, Q_3 as the control qubit pair. **d**, A conditionality

measurement, using a Ramsey-like sequence $\{R_Y^{(t)}(\frac{\pi}{2}), \text{CCZ}, R_Z^{(t)}(\phi), R_Y^{(t)}(\frac{\pi}{2})\}$, reveals the dependence of Q_1 's phase on the states of Q_2 and Q_3 under the CCZ gate implemented using the sequence in **c**, which is characteristic of a three-body entanglement. **e**, Truth table of the implemented Toffoli gate with a corresponding fidelity of 96.20(6)%. **f**, CB result showing the Pauli fidelity distributions of the three-qubit reference cycle and CCZ dressed cycle, with the solid vertical lines indicating the average values. The average gate fidelity is estimated to be 96.18(5)%.

to a continuous fSim gate set^{8,37}, which can be integrated into arbitrary quantum circuits compatible with fixed-frequency qubits by using more advanced circuit compilation tools³⁸ or efficient physical Z-gates.

Our analysis attributes the limitations of these results primarily to decoherence mechanisms (Supplementary Notes 10–12). Intriguingly, the Floquet qubits appear to exhibit coherence times deviating from those of the bare qubits, as shown in Fig. 3b. The measurements are performed using nominal energy relaxation and echo dephasing procedures on the bare Q_1 , but with the addition of a microwave pulse applied 40 MHz red-detuned from its $|0\rangle \leftrightarrow |1\rangle$ transition during idle periods. The results are postselected to yield the populations of the desired states, and the experiment is repeated over twenty iterations to eliminate any potential outlier. While the dynamics remain the same at small drive amplitudes, T_1 tends to increase while T_2^E tends to decrease at strong driving before non-adiabaticity sets in. Interestingly, we also discover a heating mechanism that enlarges the excited state population in the bare qubit at the end of the 355- μs -long $|0\rangle \rightarrow |1\rangle$ measurement sequence, with $P_{|1\rangle}^{\text{final}}$ increasing with the driving amplitude (Fig. 3b, inset). We include additional details in Supplementary Note 13 and hope that future investigations can find efficient approaches to mitigate these effects, reminiscent of the recent progress in driven ultracold-atom systems³⁹.

Floquet qutrit and three-qubit gate

So far, the fundamental and universal importance of spin physics motivates our discussion to portray the implemented Floquet qubits as ideal spin-halves. Nevertheless, many solid-state systems, including the transmon, naturally include multiple relevant energy levels. Making

use of them expands the Hilbert space, allowing more information to be encoded, which leads to hardware-efficient execution of quantum algorithms^{40,41} and hastens the development of fault-tolerant computation^{42,43}. We now show that the presented protocol can be tailored for multi-level systems, thereby paving pathways for quantum information processing using Floquet qutrits.

Specifically, we leverage the techniques described so far to induce a transverse qutrit–qutrit interaction between the states $|11\rangle$ and $|02\rangle$. Although the cross-Kerr coupling has been explored⁴⁴, such an energy-exchange interaction is still absent in fixed-frequency qutrits. While this is a useful ternary gate itself, we presently show that integrating it into a sequence involving multiple qubits allows the implementation of a three-body CCZ gate³⁰, which plays an important role in quantum applications such as factorization^{45,46} and quantum error correction^{47,48}. Notably, this scheme can be extended to implement an n -qubit gate⁴⁹. To this end, we add to the experiment Q_3 , which is coupled to the right side of Q_2 in Fig. 1a and use Q_2 and Q_3 as control qubits (subscripted c), while Q_1 is designated as the target (subscripted t).

Figure 4a depicts the energy diagram of Q_2 and Q_3 . Our approach to accomplish the interaction primarily involves applying a microwave pulse to Q_3 at a frequency red-detuned from its $|1\rangle \leftrightarrow |2\rangle$ transition to create a Floquet qutrit such that the control Floquet states $|11\rangle_c$ and $|02\rangle_c$ become degenerate. After initializing the control qubits in $|11\rangle_c$, we apply such a pulse with ramp time $\tau_r = 170$ ns, DRAG coefficient $\lambda_{\text{DRAG}} = -0.6$ and varying amplitude A_{XY} and duration τ_g , which are tailored to ensure adiabaticity at a red-detuning of 22 MHz. The transverse interaction between $|11\rangle_c$ and $|02\rangle_c$ then manifests into an asymmetric chevron pattern with respect to A_{XY} and τ_g in Fig. 4b. Interestingly, we

observe that the optimal swap condition occurs at a stronger amplitude relative to the symmetry point.

A CCZ unitary can be implemented using the sequence given in Fig. 4c (Supplementary Note 14). The final CPhase gate on the control qubits is tuned to bring the effective operation on them to be $\delta_1 \otimes \delta_1$ at the end of the sequence. After calibrating the individual gates, we verify the entanglement between the three qubits by extracting the Z-phase of the target qubit (Q_1) for different control states and observe a phase shift of approximately π for $|10\rangle_c$ (Fig. 4d), which evinces the CCZ effect. The sequence can be further sandwiched between single-qubit rotations on Q_1 to construct a Toffoli gate. The process can be straightforwardly validated by measuring the truth table^{30,49}, from which we extracted a fidelity of $\mathcal{F}_{\text{fit}} = \text{Tr}(\mathcal{U}_{\text{exp}} \mathcal{U}_{\text{ideal}}^\dagger)/8 = 96.20(6)\%$ (Fig. 4e). Finally, we employ CB to benchmark the CCZ gate (Fig. 4f), achieving a fidelity of 96.18(5)%, with the main error resulting from decoherence (Supplementary Note 11).

Outlook

Our work embodies a transformative application of Floquet engineering in superconducting circuits where periodic drives are used to map static qubits to Floquet qubits with modifiable quasienergies, granting access to an unconventional tuning channel. We demonstrate the practicality and versatility of this approach by synthesizing Floquet qubits and qutrits, then realizing an XXZ Heisenberg interaction between them with fully tunable anisotropy. The robustness of the scheme against environmental noise, non-adiabaticity, leakage and calibration errors is reflected in the high gate fidelities, while overcoming the current limitations is straightforward. On one hand, the coherence times of the fixed-frequency transmon qubits in the experiment are relatively low, so we expect better performance in state-of-the-art devices. On the other hand, the coupling rate is primarily limited by the static coupling constant J , which can be increased substantially in future devices. In addition, the pulse shape used in this work is quite simple, so we believe that, in the future, advanced STA techniques can be employed to design shorter gates, further reducing errors from dephasing. Our preliminary assessment (Supplementary Note 15) shows the promising extensibility of the protocol to large-scale devices. We note that the experimental device is simply a testbed, and the full potential of this framework lies upon its adaptation to other synthetic fixed-frequency quantum architectures with better projected performance, such as fluxonium quantum processor with all-microwave control⁵⁰.

Having illustrated the useful properties of the Floquet qubits, we envision the following avenues to further develop and propel the concept to scale up fixed-frequency platforms. The protocol presented here involves transforming back to the static qubit, so normal operations such as readout and single-qubit gates can be employed without recalibration. In future applications, a Floquet qubit can, in principle, be permanently defined by applying a continuous periodic drive, streamlining the process and unlocking opportunities for control and readout of the Floquet qubit²⁵ (Supplementary Note 16). This approach also allows in situ tuning of the qubit frequencies, thus providing a practical solution for problems arising from two-level-system defects and spectral crowding. Alternatively, the ramp time can be reduced substantially if we operate in the diabatic regime, where the mapping is close to ideal despite finite transition between the Floquet states. We expect the potential development of optimal control within the Floquet framework to provide a reliable approach in this regime. Last but not least, the heating effect which correlates with the reduction in T_2 is reminiscent of a similar effect in cold-atom systems which has been successfully suppressed³⁹. This calls for deeper understanding of the quantum thermodynamics in driven solid-state systems and the development of new mitigation strategies.

Online content

Any methods, additional references, Nature Portfolio reporting summaries, source data, extended data, supplementary information,

acknowledgements, peer review information; details of author contributions and competing interests; and statements of data and code availability are available at <https://doi.org/10.1038/s41567-023-02326-7>.

References

- Salathé, Y. et al. Digital quantum simulation of spin Models with circuit quantum electrodynamics. *Phys. Rev. X* **5**, 021027 (2015).
- Savary, L. & Balents, L. Quantum spin liquids: a review. *Rep. Prog. Phys.* **80**, 016502 (2016).
- Bernien, H. et al. Probing many-body dynamics on a 51-atom quantum simulator. *Nature* **551**, 579 (2017).
- Jepsen, P. N. et al. Spin transport in a tunable Heisenberg model realized with ultracold atoms. *Nature* **588**, 403 (2020).
- Zhang, J. et al. Observation of a discrete time crystal. *Nature* **543**, 217 (2017).
- Jepsen, P. N. et al. Long-lived phantom helix states in Heisenberg quantum magnets. *Nat. Phys.* **18**, 899 (2022).
- Morvan, A. et al. Formation of robust bound states of interacting microwave photons. *Nature* **612**, 240 (2022).
- Kivlichan, I. D. et al. Quantum simulation of electronic structure with linear depth and connectivity. *Phys. Rev. Lett.* **120**, 110501 (2018).
- Bharti, K. et al. Noisy intermediate-scale quantum algorithms. *Rev. Mod. Phys.* **94**, 015004 (2022).
- Fowler, A. G. et al. Surface codes: towards practical large-scale quantum computation. *Phys. Rev. A* **86**, 032324 (2012).
- Ghosh, J. & Fowler, A. G. Leakage-resilient approach to fault-tolerant quantum computing with superconducting elements. *Phys. Rev. A* **91**, 020302 (2015).
- Koch, J. et al. Charge-insensitive qubit design derived from the Cooper pair box. *Phys. Rev. A* **76**, 042319 (2007).
- Paik, H. et al. Observation of high coherence in Josephson junction qubits measured in a three-dimensional circuit QED architecture. *Phys. Rev. Lett.* **107**, 240501 (2011).
- Manucharyan, V. E. et al. Fluxonium: single Cooper-pair circuit free of charge offsets. *Science* **326**, 113 (2009).
- Nguyen, L. B. et al. High-coherence fluxonium qubit. *Phys. Rev. X* **9**, 041041 (2019).
- Chow, J. M. et al. Simple all-microwave entangling gate for fixed-frequency superconducting qubits. *Phys. Rev. Lett.* **107**, 080502 (2011).
- Kim, Y. et al. High-fidelity three-qubit iToffoli gate for fixed-frequency superconducting qubits. *Nat. Phys.* **18**, 783 (2022).
- Mitchell, B. K. et al. Hardware-efficient microwave-activated tunable coupling between superconducting qubits. *Phys. Rev. Lett.* **127**, 200502 (2021).
- Wei, K. X. et al. Hamiltonian engineering with multicolor drives for fast entangling gates and quantum crosstalk cancellation. *Phys. Rev. Lett.* **129**, 060501 (2022).
- Collodo, M. C. et al. Implementation of conditional phase gates based on tunable ZZ interactions. *Phys. Rev. Lett.* **125**, 240502 (2020).
- Xu, Y. et al. High-fidelity, high-scalability two-qubit gate scheme for superconducting qubits. *Phys. Rev. Lett.* **125**, 240503 (2020).
- Stehlik, J. et al. Tunable coupling architecture for fixed-frequency transmon superconducting qubits. *Phys. Rev. Lett.* **127**, 080505 (2021).
- Ganzhorn, M. et al. Benchmarking the noise sensitivity of different parametric two-qubit gates in a single superconducting quantum computing platform. *Phys. Rev. Res.* **2**, 033447 (2020).
- Huang, Z. et al. Engineering dynamical sweet spots to protect qubits from $1/f$ noise. *Phys. Rev. Appl.* **15**, 034065 (2021).
- Gandon, A. et al. Engineering, control, and longitudinal readout of Floquet qubits. *Phys. Rev. Appl.* **17**, 064006 (2022).

26. Sameti, M. & Hartmann, M. J. Floquet engineering in superconducting circuits: from arbitrary spin-spin interactions to the Kitaev honeycomb model. *Phys. Rev. A* **99**, 012333 (2019).
27. Guéry-Odelin, D. et al. Shortcuts to adiabaticity: concepts, methods, and applications. *Rev. Mod. Phys.* **91**, 045001 (2019).
28. Motzoi, F. et al. Simple pulses for elimination of leakage in weakly nonlinear qubits. *Phys. Rev. Lett.* **103**, 110501 (2009).
29. Gambetta, J. M. et al. Analytic control methods for high-fidelity unitary operations in a weakly nonlinear oscillator. *Phys. Rev. A* **83**, 012308 (2011).
30. Fedorov, A. et al. Implementation of a Toffoli gate with superconducting circuits. *Nature* **481**, 170 (2012).
31. Majer, J. et al. Coupling superconducting qubits via a cavity bus. *Nature* **449**, 443 (2007).
32. Blais, A. et al. Circuit quantum electrodynamics. *Rev. Mod. Phys.* **93**, 025005 (2021).
33. Weitenberg, C. & Simonet, J. Tailoring quantum gases by Floquet engineering. *Nat. Phys.* **17**, 1342 (2021).
34. Shirley, J. H. Solution of the Schrödinger equation with a Hamiltonian periodic in time. *Phys. Rev.* **138**, B979 (1965).
35. Deng, C. et al. Dynamics of a two-level system under strong driving: quantum-gate optimization based on Floquet theory. *Phys. Rev. A* **94**, 032323 (2016).
36. Erhard, A. et al. Characterizing large-scale quantum computers via cycle benchmarking. *Nat. Commun.* **10**, 5347 (2019).
37. Foxen, B. et al. Demonstrating a continuous set of two-qubit gates for near-term quantum algorithms. *Phys. Rev. Lett.* **125**, 120504 (2020).
38. Chen, J. et al. Compiling arbitrary single-qubit gates via the phase shifts of microwave pulses. *Phys. Rev. Res.* **5**, L022031 (2023).
39. Viebahn, K. et al. Suppressing dissipation in a Floquet-Hubbard system. *Phys. Rev. X* **11**, 011057 (2021).
40. Bocharov, A., Roetteler, M. & Svore, K. M. Factoring with qutrits: Shor's algorithm on ternary and metaplectic quantum architectures. *Phys. Rev. A* **96**, 012306 (2017).
41. Gokhale, P. et al. Asymptotic improvements to quantum circuits via qutrits. In *Proc. 46th International Symposium on Computer Architecture* 554–566 (ACM, 2019).
42. Campbell, E. T. Enhanced fault-tolerant quantum computing in *d*-level systems. *Phys. Rev. Lett.* **113**, 230501 (2014).
43. Muralidharan, S. et al. Overcoming erasure errors with multilevel systems. *New J. Phys.* **19**, 013026 (2017).
44. Goss, N. et al. High-fidelity qutrit entangling gates for superconducting circuits. *Nat. Commun.* **13**, 7481 (2022).
45. Shor, P. W. Polynomial-time algorithms for prime factorization and discrete logarithms on a quantum computer. *SIAM J. Comput.* **26**, 1484 (1997).
46. Gidney, C. & Ekerå, M. How to factor 2048 bit RSA integers in 8 hours using 20 million noisy qubits. *Quantum* **5**, 433 (2021).
47. Yoder, T. J., Takagi, R. & Chuang, I. L. Universal fault-tolerant gates on concatenated stabilizer codes. *Phys. Rev. X* **6**, 031039 (2016).
48. Chao, R. & Reichardt, B. W. Fault-tolerant quantum computation with few qubits. *npj Quantum Inf.* **4**, 42 (2018).
49. Chu, J. et al. Scalable algorithm simplification using quantum AND logic. *Nat. Phys.* **19**, 126 (2023).
50. Nguyen, L. B. et al. Blueprint for a high-performance fluxonium quantum processor. *PRX Quantum* **3**, 037001 (2022).

Publisher's note Springer Nature remains neutral with regard to jurisdictional claims in published maps and institutional affiliations.

Open Access This article is licensed under a Creative Commons Attribution 4.0 International License, which permits use, sharing, adaptation, distribution and reproduction in any medium or format, as long as you give appropriate credit to the original author(s) and the source, provide a link to the Creative Commons license, and indicate if changes were made. The images or other third party material in this article are included in the article's Creative Commons license, unless indicated otherwise in a credit line to the material. If material is not included in the article's Creative Commons license and your intended use is not permitted by statutory regulation or exceeds the permitted use, you will need to obtain permission directly from the copyright holder. To view a copy of this license, visit <http://creativecommons.org/licenses/by/4.0/>.

© The Author(s) 2024

Data availability

All analysed data are available at <https://doi.org/10.6084/m9.figshare.24217011.v1>. Source data are provided with this paper. All other data that support the findings of this study are available from the corresponding authors upon reasonable request.

Acknowledgements

We thank A. Morvan and W. P. Livingston for their assistance with the measurement. L.B.N. is grateful to Z. Huang, I. Mondragon-Shem and J. Koch for valuable discussions on Floquet theory. The micrograph of the chip was obtained with support from B. Qing and K. Lee. This work was supported by the Office of Advanced Scientific Computing Research, Testbeds for Science programme, Office of Science of the US Department of Energy under Contract No. DE-AC02-05CH11231, the KIST research programme under grant No. 2E32241 and ARO grant No. W911NF-22-1-0258.

Author contributions

L.B.N. conceived and organized the project. Y.K. initiated the measurement and applied the Floquet framework. L.B.N. and Y.K. acquired the data and analysed the results. A.H. assisted with device calibration and CB evaluation. N.G. assisted with the characterization of qutrits and the CCZ gate. B.M. assisted with cross-entropy

benchmarking. B.B. and D.D. assisted with Floquet theory. R.K.N. set up the microwave apparatus. J.M.K. fabricated the device. A.N.J. supervised the theoretical work. D.I.S. and I.S. oversaw the experimental effort. L.B.N. and Y.K. wrote the paper with input from A.H., N.G. and B.B.

Competing interests

The authors declare no competing interests.

Additional information

Supplementary information The online version contains supplementary material available at <https://doi.org/10.1038/s41567-023-02326-7>.

Correspondence and requests for materials should be addressed to Long B. Nguyen or Yosep Kim.

Peer review information *Nature Physics* thanks Michael Hartmann and the other, anonymous, reviewer(s) for their contribution to the peer review of this work.

Reprints and permissions information is available at www.nature.com/reprints.